

Origin of nonlinearity and plausible turbulence by hydromagnetic transient growth in accretion disks: Faster growth rate than magnetorotational instability

Sujit Kumar Nath, Banibrata Mukhopadhyay*

Department of Physics, Indian Institute of Science, Bangalore 560012, India

sujitkumar@physics.iisc.ernet.in, bm@physics.iisc.ernet.in

*Corresponding author

We investigate the evolution of hydromagnetic perturbations in a small section of accretion disks. It is known that molecular viscosity is negligible in accretion disks. Hence, it has been argued that a mechanism, known as Magnetorotational Instability (MRI), is responsible for transporting matter in the presence of weak magnetic field. However, there are some shortcomings, which question effectiveness of MRI. Now the question arises, whether other hydromagnetic effects, e.g. transient growth (TG), can play important role to bring nonlinearity in the system, even at weak magnetic fields. Otherwise, whether MRI or TG, which is primarily responsible to reveal nonlinearity to make the flow turbulent? Our results prove explicitly that the flows with high Reynolds number (R_e), which is the case of realistic astrophysical accretion disks, exhibit nonlinearity by TG of perturbation modes faster than that by modes producing MRI. For a fixed wavevector, MRI dominates over transient effects, only at low R_e , lower than its value expected to be in astrophysical accretion disks, and low magnetic fields. This seriously questions (overall) suaveness of MRI in astrophysical accretion disks.

PACS: 98.62.Mw, 95.30.Qd, 47.27.T-, 47.35.Tv

I. INTRODUCTION

Accretion disks are found in active galactic nuclei (AGNs), around compact stellar objects in a binary system, around newly formed stars etc. (see, e.g., [1]). However, the working principle of accretion disks still remains enigmatic to us. Due to its inadequacy of molecular viscosity, turbulent viscosity has been proposed to explain the transport of matter towards the central object. This idea is particularly attractive because of its high Reynolds number $R_e \gtrsim 10^{14}$ (see, e.g., [2]). However, the Keplerian disks, which are relevant to many astrophysical applications, are remarkably Rayleigh stable. Therefore, linear perturbation cannot induce the onset of turbulence, and consequently cannot provide enough viscosity to transport matter inwards therein.

With the application of Magnetorotational Instability (MRI; [3, 4]) to Keplerian disks, Balbus & Hawley [5] showed that initial seed, weak magnetic field can lead to the velocity and magnetic field perturbations growing exponentially. Within a few rotation times, such exponential growth could reveal the onset of turbulence. Since then, MRI has been a widely accepted mechanism to explain origin of instability and hence transport of matter in accretion disks. Note that for flows having strong magnetic fields, where the magnetic field is tightly coupled with the flow, MRI is not expected to work. Hence, it is very clear that the MRI is bounded in a small regime of parameter values when field is weak.

It has been well established by several works that transient growth (TG) can reveal nonlinearity and transition to turbulence at sub-critical R_e (e.g. [6–11]). Such sub-critical transition to turbulence was invoked to explain colder purely hydrodynamic accretion flows e.g. quiescent cataclysmic variables, in proto-planetary and star-forming disks, the outer region of disks in active galactic nuclei. Baroclinic instability is another plausible source for vigorous turbulence in colder accretion disks [12]. Note that while hotter flows are expected to be ionized enough to produce weak magnetic fields therein and subsequent MRI, colder flows may remain to be practically neutral in charge and hence any instability and turbulence therein must be hydrodynamic. However, in the absence of magnetic effects, the Coriolis force does not allow any significant TG in accretion disks in three dimensions, independent of R_e (see [6]), while in pure two dimensions TG could be large at large R_e . However, a pure two-dimensional flow is a very idealistic case. Nevertheless, in the presence of magnetic field, even in three dimensions, TG could be very large (Coriolis effects could not suppress the growth). Hence, in a real three-dimensional flow, it is very important to explore magnetic TG.

In the present paper, we explore the relative strengths of MRI and TG in magnetized accretion flows, in order to explain the generic origin of nonlinearity and plausible turbulence therein. By TG we precisely mean the short-time scale growth due to shearing perturbation waves, producing a peak followed by a dip. By MRI we mean the exponential growth by static perturbation waves. While TG may reveal nonlinearity in the system, depending on R_e ,

amplitude of initial perturbation and its wavevector and background rotational profile of the flow, question is, can its growth rate be fast enough to compete with that of MRI? On the other hand, is there any limitation of MRI, apart from the fact that MRI does not work at strong magnetic fields? Note that some limitations of MRI were already discussed by previous authors [11, 13–16], which then question the origin of viscosity in accretion disks.

We show below that the three-dimensional TG dominates over the growth due to MRI modes at large R_e , bringing nonlinearity in the flows. This is of immense interest, as the larger R_e is more plausible in accretion disks. By comparing modes corresponding to static (original MRI) and shearing (TG) waves, the growth estimates from static MRI waves have already been argued to be misleading [17]. Throughout their work, previous authors [17] argued that shearing wave structures always grow faster over short time scales than static structures, what we also plan to elaborate here. Nevertheless, those authors [17] did not explore the length of time over which the short-time growth can persist, which is very important for revealing non-linearity, which we plan to explicitly explore here. We will show below that in a shorter time-scale, TG reveals nonlinearity into the system.

We explicitly calculate the magnetic field strength above which MRI not working. Moreover, for a fixed perturbation (which might not be either corresponding to the best MRI or best TG mode) with finite R_e , with the increase of R_e , we show that the TG tends to bring the nonlinearity in the systems before MRI could do the same, producing a large growth of perturbation. We notice that above a threshold R_e , only TG is sufficient to make the system nonlinear at low magnetic field and there is no growth at high magnetic fields. Hence, in the regimes of high magnetic field or/and high R_e , MRI is not important at all. The working regime of MRI is rather much narrower than it is generally thought off. As TG was argued to be plausible source of nonlinearity in cold disks and the growth due to MRI is subdominant compared to TG at high R_e in hot disks, TG could be argued to be the source of nonlinearity and plausible turbulence and subsequent viscosity, in any accretion disk.

In the next section, we discuss the perturbation equations describing flows. Subsequently, we explore total energy growths of perturbations due to TG and MRI for different parameter values and, furthermore, compare the respective parameter spaces for different initial amplitudes of perturbations in §III and §IV respectively. Finally we end with a discussion in §V.

II. GOVERNING EQUATIONS DESCRIBING MAGNETIZED ROTATING SHEAR FLOWS IN LAGRANGIAN COORDINATES

Within a local shearing box, in Lagrangian coordinate, the Navier-Stokes, continuity, magnetic induction equations and solenoidal condition (for magnetic field) can be written as

$$\dot{\mathbf{v}} = -\frac{1}{\rho}c_s^2\nabla\rho + \nu\nabla^2\mathbf{v} + 2\mathbf{v} \times \boldsymbol{\Omega} + \frac{1}{4\pi\rho}\mathbf{B} \cdot \nabla\mathbf{B}, \quad (1)$$

$$\frac{d\rho}{dt} = -\rho\nabla \cdot \mathbf{v}, \quad (2)$$

$$\frac{\partial\mathbf{B}}{\partial t} = \nabla \times (\mathbf{v} \times \mathbf{B}), \quad \nabla \cdot \mathbf{B} = 0, \quad (3)$$

when

$$\dot{\mathbf{r}} = \mathbf{v}(\mathbf{r}^L), \quad \nabla \equiv \frac{\partial\mathbf{r}^L}{\partial\mathbf{r}} \cdot \nabla^L, \quad (4)$$

where \mathbf{v} is the velocity vector, \mathbf{B} the magnetic field, ν the kinematic coefficient of viscosity, c_s the sound speed in the shearing box, $\boldsymbol{\Omega}$ the angular velocity, ρ the density, \mathbf{r} and \mathbf{r}^L are the position vectors in Eulerian and Lagrangian coordinates respectively [7]. Note that the contribution of magnetic pressure has been included to the total pressure in the first term in the right hand side of equation (1). For incompressible flow, equation (2) becomes

$$\nabla \cdot \mathbf{v} = 0. \quad (5)$$

Let us define the tensor $\Omega\mathbf{q}$ which is the minus of the gradient of the unperturbed (background) velocity field $\mathbf{v}_0 = (0, -q\Omega x, 0)$ as

$$\Omega\mathbf{q} \equiv -\nabla\mathbf{v}_0 = -(\nabla\boldsymbol{\Omega}) \times \mathbf{R} = \begin{pmatrix} 0 & q\Omega & 0 \\ 0 & 0 & 0 \\ 0 & 0 & 0 \end{pmatrix}; \quad q = -\frac{d\ln\Omega}{d\ln R}, \quad (6)$$

where $\mathbf{R} = (R, 0, 0)$ and R is the distance of the comoving shearing box from the center of the disk and $|\mathbf{\Omega}| = \Omega \propto R^{-q}$ (see [7] for details). Now integrating equation (4), we obtain

$$\mathbf{r}^L = \mathbf{r} + \Omega t \mathbf{r} \cdot \mathbf{q} \Rightarrow \frac{\partial \mathbf{r}^L}{\partial \mathbf{r}} = \mathbf{1} + \Omega t \mathbf{q}, \quad (7)$$

and this gives rise to the relation

$$\nabla \equiv (\mathbf{1} + \Omega t \mathbf{q}) \cdot \nabla^L. \quad (8)$$

Since the unperturbed velocity \mathbf{v}_0 has spatial dependence, it has a nonvanishing time derivative in perturbed Lagrangian coordinate. Therefore, we obtain

$$\dot{\delta \mathbf{v}} = \dot{\mathbf{v}} - \dot{\mathbf{v}}_0 = \dot{\mathbf{v}} - \mathbf{v} \cdot \nabla \mathbf{v}_0 = \dot{\mathbf{v}} + \Omega \mathbf{v} \cdot \mathbf{q}. \quad (9)$$

Perturbing and linearizing equations (1), (2), (3) and using equation (9), we obtain the perturbed Navier-Stokes, continuity, induction equations and solenoidal equation for magnetic field in Lagrangian coordinate as

$$\dot{\delta \mathbf{v}} = -\frac{1}{\rho} c_s^2 \nabla \delta \rho + \nu \nabla^2 \delta \mathbf{v} + 2 \delta \mathbf{v} \times \mathbf{\Omega} + \frac{1}{4\pi \rho} \mathbf{B} \cdot \nabla \delta \mathbf{B} + \Omega \delta \mathbf{v} \cdot \mathbf{q}, \quad (10)$$

$$\dot{\delta \rho} = -\rho \nabla \cdot \delta \mathbf{v}, \quad (11)$$

$$\dot{\delta \mathbf{B}} = \nabla \times (\mathbf{v} \times \delta \mathbf{B} + \delta \mathbf{v} \times \mathbf{B}) + (\mathbf{v} \cdot \nabla) \delta \mathbf{B}, \quad \nabla \cdot \delta \mathbf{B} = 0, \quad (12)$$

where $\delta \mathbf{v}$, $\delta \mathbf{B}$ and $\delta \rho$ are the velocity, magnetic field vectors and the density of perturbation respectively.

We now work with the incompressible approximation, i.e. $\delta \rho \rightarrow 0$ and $c_s^2 \rightarrow \infty$, assuming $c_s^2 \delta \rho$ to be finite and decomposing the general linear perturbations into a plane wave form as

$$\delta \mathbf{v}, \delta \mathbf{B} \propto \exp(i \mathbf{k}^L \cdot \mathbf{r}^L), \quad (13)$$

when

$$\mathbf{k} = (k_x, k_y, k_z) = (\mathbf{1} + \Omega t \mathbf{q}) \cdot \mathbf{k}^L = (k_x^L + q \Omega t k_y^L, k_y^L, k_z^L), \quad (14)$$

where \mathbf{k} and \mathbf{k}^L are the wavevectors in the Eulerian and Lagrangian coordinates respectively. Now using solenoidal condition for magnetic field, incompressibility condition and plane wave solution (13), and if we write equations (10) and (12) (i.e. Navier-Stokes and magnetic induction equations) componentwise, we obtain

$$\delta \dot{v}_x = -i \frac{1}{\rho} c_s^2 \delta \rho (k_x^L + q \Omega t k_y^L) - \nu k^2 \delta v_x + 2 \Omega \delta v_y + \frac{1}{4\pi \rho} i \delta B_x (B_1 k_x + B_2 k_y + B_3 k_z), \quad (15)$$

$$\delta \dot{v}_y = -i \frac{1}{\rho} c_s^2 \delta \rho k_y^L - \nu k^2 \delta v_y - 2 \Omega \delta v_x + \Omega q \delta v_x + \frac{1}{4\pi \rho} i \delta B_y (B_1 k_x + B_2 k_y + B_3 k_z), \quad (16)$$

$$\delta \dot{v}_z = -i \frac{1}{\rho} c_s^2 \delta \rho k_z^L - \nu k^2 \delta v_z + \frac{1}{4\pi \rho} i \delta B_z (B_1 k_x + B_2 k_y + B_3 k_z), \quad (17)$$

$$\delta \dot{B}_x = i \delta v_x (B_1 k_x + B_2 k_y + B_3 k_z), \quad (18)$$

$$\delta \dot{B}_y = i \delta v_y (B_1 k_x + B_2 k_y + B_3 k_z) - q \Omega \delta B_x, \quad (19)$$

$$\delta \dot{B}_z = i \delta v_z (B_1 k_x + B_2 k_y + B_3 k_z). \quad (20)$$

For the convenience of solutions, we further define

$$\Delta = k_x \delta v_x + k_y \delta v_y, \zeta = k_x \delta v_y - k_y \delta v_x, \Delta_B = k_x \delta B_x + k_y \delta B_y, \zeta_B = k_x \delta B_y - k_y \delta B_x,$$

and for the plane wave solutions given by equation (13), equations (15)-(20) can be recast into

$$\begin{pmatrix} \dot{\Delta} \\ \dot{\zeta} \\ \dot{\Delta}_B \\ \dot{\zeta}_B \end{pmatrix} = \begin{pmatrix} M_{11} & M_{12} & M_{13} & M_{14} \\ M_{21} & M_{22} & M_{23} & M_{24} \\ M_{31} & M_{32} & M_{33} & M_{34} \\ M_{41} & M_{42} & M_{43} & M_{44} \end{pmatrix} \begin{pmatrix} \Delta \\ \zeta \\ \Delta_B \\ \zeta_B \end{pmatrix}, \quad (21)$$

where

$$\begin{aligned} M_{11} &= \frac{-\nu k^4(k_x^2 + k_y^2) + 2q\Omega k_x k_y k_z^2}{k^2(k_x^2 + k_y^2)}, \quad M_{12} = \frac{2\Omega k_z^2\{k_x^2 + (1-q)k_y^2\}}{k^2(k_x^2 + k_y^2)}, \\ M_{13} &= \frac{i(B_1 k_x + B_2 k_y + B_3 k_z)}{4\pi\rho}, \quad M_{14} = 0, \\ M_{21} &= \Omega(q-2), \quad M_{22} = -\nu k^2, \quad M_{23} = 0, \quad M_{24} = \frac{i(B_1 k_x + B_2 k_y + B_3 k_z)}{4\pi\rho}, \\ M_{31} &= i(B_1 k_x + B_2 k_y + B_3 k_z), \quad M_{32} = 0, \quad M_{33} = 0, \quad M_{34} = 0, \\ M_{41} &= 0, \quad M_{42} = i(B_1 k_x + B_2 k_y + B_3 k_z), \quad M_{43} = \frac{q\Omega(k_y^2 - k_x^2)}{k_x^2 + k_y^2}, \quad M_{44} = \frac{2q\Omega k_x k_y}{k_x^2 + k_y^2}. \end{aligned}$$

The assumption of incompressibility is justified as follows. If the wavelength of the velocity perturbations is much shorter than the sound horizon for the time of interest (which is in the present context the infall time of matter), then the density perturbations (which is basically the sound waves) reach equilibrium early on, which renders effectively a uniform density during the timescale of interest. For an astrophysical accretion disk around a black hole, which is either geometrically thin or can be approximated as a vertically averaged flow, the half-thickness of the disk is comparable to the sound horizon corresponding to one disk rotation time. Therefore, as described in previous work (e.g. [7]), for processes taking longer than one rotation time, wavelengths shorter than the disk thickness can be approximately treated as incompressible.

Solving the set of differential equations (21), we can calculate $\delta\mathbf{v}$, $\delta\mathbf{B}$ and the energy \mathcal{E} of the perturbation given by

$$\mathcal{E} \propto \left(\delta\mathbf{v}^2 + \frac{\delta\mathbf{B}^2}{4\pi\rho} \right) = \left(\frac{4\pi\rho(\Delta^2 + \zeta^2) + \Delta_B^2 + \zeta_B^2}{(k_x + k_y q t \Omega)^2 + k_y^2} + \frac{4\pi\Delta^2\rho + \Delta_B^2}{k_z^2} \right) / 8\pi\rho, \quad (22)$$

in terms of new variables. In order to solve the set of equations (21), we have to supply $\delta\mathbf{B}$ and $\delta\mathbf{v}$ at $t = 0$, i.e. initial perturbation amplitude (IPA). The structure (and evolution) of perturbations are similar/same as that found earlier [6, 7, 17]. A sample is shown in Fig. 1, demonstrating how an initial leading wave, with a highly stretched structure, evolves to a spherical wave at the maximum of TG and furthermore evolves to a trailing wave, during the declining phase of TG. During this evolution of perturbation, observing the associated total energy growth of perturbation, we now plan to understand whether the perturbation will sustain or not to give rise to nonlinearity and plausible turbulence and essentially viscosity to help infall of matter in an accretion disk. By a detailed investigation, we can also understand the relative weight between TG and growth due to MRI (if at all working) in the time of interest. Moreover, we plan to pinpoint the limit of magnetic field strength, above which the MRI is suppressed (indeed MRI works only for weak magnetic fields).

III. TOTAL ENERGY GROWTH OF PERTURBATIONS FOR DIFFERENT PARAMETER VALUES

The best possible mode for MRI giving rise to the nonlinearity into the system corresponds to the condition $k_z v_{Az} / \Omega = 1$ (when $v_{Az}^2 = B_z^2 / 4\pi\rho$) [5]. The growth rate for this fastest exponentially growing mode is $3\Omega/4 = 3/4q$ (since in dimensionless unit $\Omega = 1/q$) [5, 6, 18]. Is there any mode for which TG brings in the nonlinearity into the flow (the best possible mode for TG) at a timescale shorter than the rotational time at which the best possible MRI mode brings in the nonlinearity? Note that an approximate emergence of nonlinearity is defined through the measurement

$$\text{Linearity} = \left(\frac{|\delta\mathbf{v}|}{|\mathbf{v}|} + \frac{|\delta\mathbf{B}|}{|\mathbf{B}|} \right). \quad (23)$$

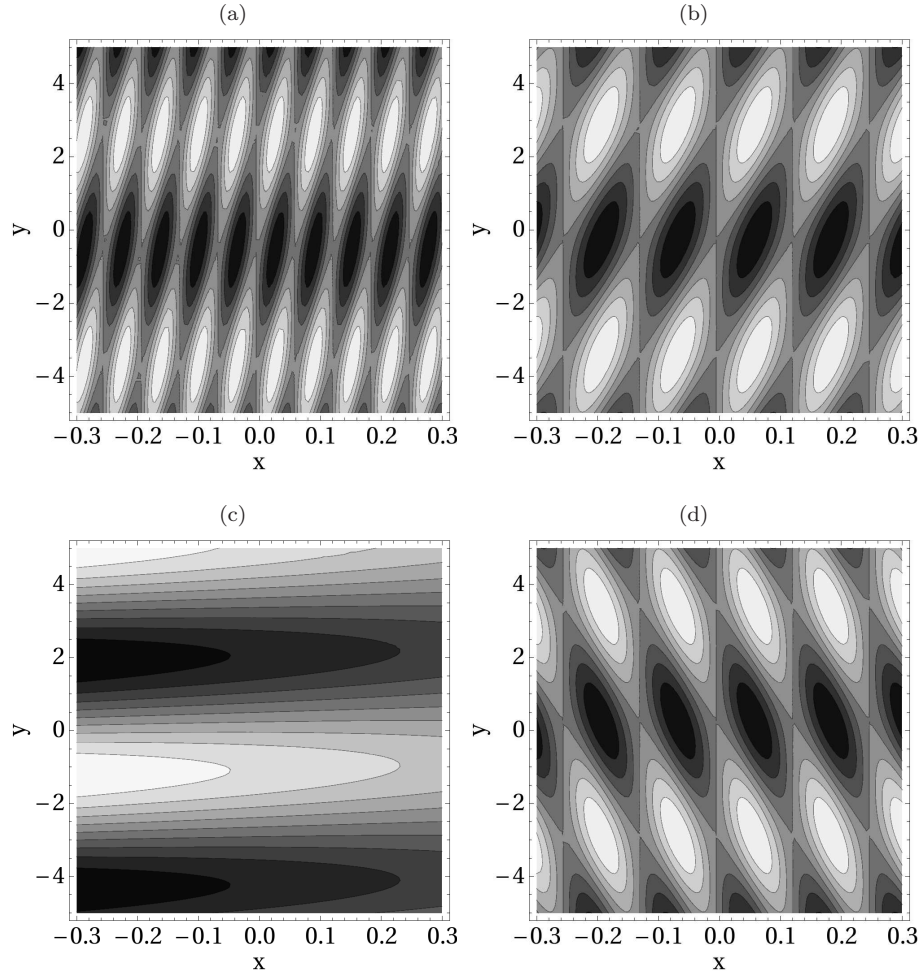


FIG. 1: Development of the perturbed velocity $\delta v_x(x, y)$ as a function of time, when $R_e = 10^6$, $k_y = 1$, $z = 0$ and t_{max} denotes the time at which growth attains its maximum, at (a) $t = 0$, (b) $t_{max}/2$, (c) t_{max} and (d) $3t_{max}/2$. The gradual conversion of contour colors from white to black corresponds to the gradual conversion from positive to negative values of $\delta v_x(x, y)$ respectively.

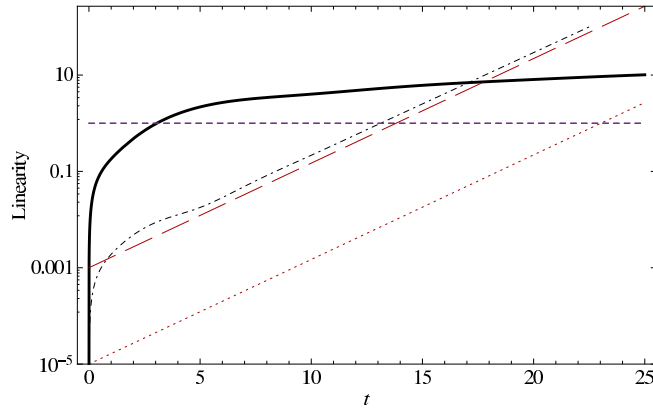


FIG. 2: (Color online) Nonlinearity via best possible TG and MRI. Thick black line corresponds to the TG for $IPA = 10^{-3}$, $R_e = 10^{14}$, $k_x^L = -R_e^{1/3}$, $k_y = 1$, $k_z = 90K_x^L$; dotdashed black line corresponds to the TG for $IPA = 10^{-5}$, $R_e = 10^{25}$, $k_x^L = -R_e^{1/3}$, $k_y = 1$, $k_z = 90K_x^L$; red longdashed and dotted lines correspond to the best possible MRI starting from $IPA = 10^{-3}$ and 10^{-5} respectively. Dashed horizontal line indicates linearity unity.

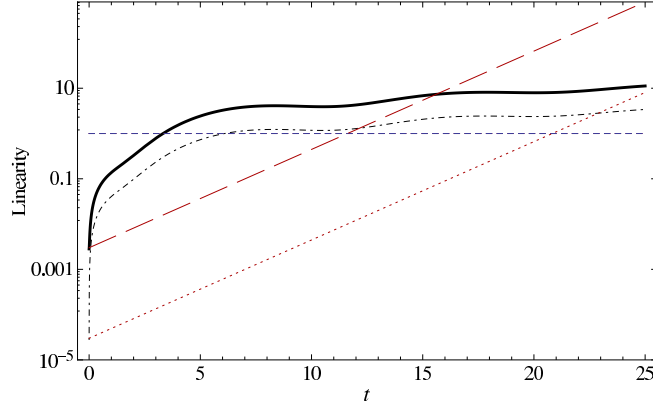


FIG. 3: Same as Fig. 2, but the black thick and dotted lines correspond to the TG for $k_x^L = 1$, $k_y = 1$, $k_z = 100$, $R_e = 10^{12}$. and $k_x^L = 1$, $k_y = 1$, $k_z = 3000$, $R_e = 10^{12}$ respectively.

When Linearity=1, the system will start becoming nonlinear which will plausibly lead to turbulence. For a Keplerian disk ($q = 3/2$), the best MRI mode brings in the nonlinearity at the timescales ~ 14 and 23 respectively for IPAs $= 10^{-3}$ and 10^{-5} (when $\log(1/\text{IPA}) = 3t/4q$). Figure 2 shows that indeed there are modes which reveal nonlinearity via TG at around 3 and 13 rotational times for IPAs 10^{-3} and 10^{-5} respectively (where $|\delta \mathbf{v}(0)|/|\mathbf{v}|, |\delta \mathbf{B}(0)|/|\mathbf{B}| = \text{IPA}$). Note from [6] that the maximum TG in two dimensions scales as $\text{TG}_{\text{max}} \sim R_e^{2/3}$ and the corresponding time as $R_e^{1/3}$ in pure hydrodynamical disks. This further corresponds to $k_x^L \sim -R_e^{1/3}$ [19], which reveals TG_{max} corresponds to the minimum of k_x , $k_{x,\text{min}}$ [6, 7]. In the same spirit, k_x^L s in Fig. 2 are chosen to be $-R_e^{1/3}$, when initial perturbations are highly stretched and nonspherical. Note that although such a stretched initial wave vector of perturbation is a special choice which is important for the present purpose, nothing prevents them to be arising in nature. Since every perturbation mode is equally probable when a system is perturbed (which is indeed the idea behind the choice of the best MRI mode), we explore the mode which is growing faster and leading the system to nonlinearity. In Fig. 3, we relax this R_e dependence of k_x^L , but still obtain the nonlinearity arising at ~ 3.5 and ~ 6 rotational times for IPAs 10^{-3} and 10^{-5} respectively. Hence, the full-scale general hydromagnetic effects giving rise to TG reveal nonlinearity into the system faster than that the MRI does, when MRI itself is uncertain. Once the best TG reveals nonlinearity before the best MRI would do, the importance of MRI is sluggish in the linear theory. Note that our current emphasis, in particular, is the arising of nonlinearity via either TG or MRI. However, nonlinearity does not guarantee the transition to turbulence, in the physical time scale of accretion. One could argue that MRI modes grow forever and, hence, the system would have been turbulent at some point, even if the best MRI modes are not considered when TG would eventually decay. But the important fact to notice here is that as soon as the system becomes nonlinear, MRI (and also TG, if that wins over MRI) is no longer applicable, as the underlying solution itself is based on linear theory. On the other hand, the effects due to the best possible MRI mode should be compared with that of the best possible TG. Such a comparison shows that TG is more powerful and is actually responsible for bringing nonlinearity into the systems.

Let us move on to the detailed behaviors of TG. In Fig. 4, we show energy growths ($\mathcal{E}(t)/\mathcal{E}(0)$) for four sets of R_e and B^2/ρ (plotted in dimensionless units, based on the dimensions of various quantities of shearing box). We see that for a fixed R_e , energy growth of perturbation decays over time if the background magnetic field is large (thick and longdashed lines compared to the dotted and dotted lines respectively). Figure 5 shows the linearity of respective cases based on equation (23). The most important point to be noted from Fig. 5 is that the case of high R_e and low \mathbf{B} (dotted line) exhibits nonlinearity via TG itself, for $\text{IPA} \approx 10^{-3}$. Note the clear appearance of TG peak in the linearity as well as growth curves at time $t \sim 10^4$. Later, at the trailing phase of TG, growth further starts increasing due to MRI. However, by this time, the system would already become nonlinear, and hence computations of energy growth and that due to MRI based on the linear theory lose their meaning. However, for a lower R_e for the same \mathbf{B} , growth due to MRI overpowers TG and nonlinearity arises via MRI induced growth (dotted line).

In order to understand a global picture and the relative powers of TG and MRI, we perform several numerical experiments and in Fig. 6 we divide the entire parameter space into three regions: MRI active, TG active and stable (or linear) zones, for a given perturbation wavevector. Note that for a given \mathbf{B} , the difference of $\log(R_e)$ between two successive computations is chosen to be unity and hence the curve dividing the linearly stable (no energy growth of perturbations) and unstable zones does not appear very smooth. The region left to the solid vertical line exhibits nonlinearity via MRI, while that of right side corresponds to nonlinearity via TG before MRI could kick in.

Hence, a very important message here is that energy growth rate due to MRI is faster than TG only at lower values

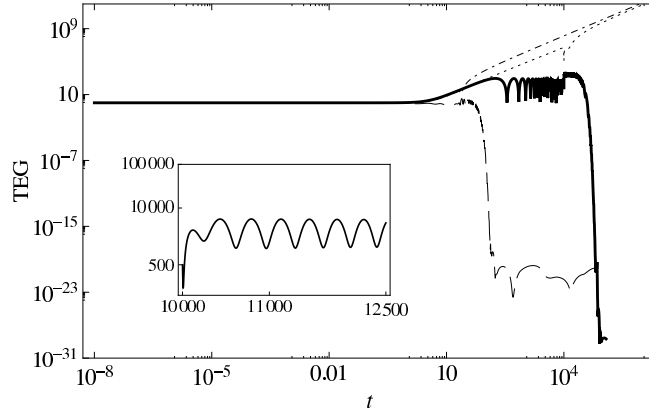


FIG. 4: Total energy growth for different sets of R_e and $\mathbf{B} = (0, 0, B_3)$: Thick, longdashed, dotted and dotdashed lines correspond to respectively $R_e = 10^{12}$ and $B^2/\rho = 10^{-3}$, $R_e = 10^4$ and $B^2/\rho = 10$, $R_e = 10^{12}$ and $B^2/\rho = 10^{-20}$ and $R_e = 10^4$ and $B^2/\rho = 10^{-20}$. $k_x^L = -R_e^{1/3}$, $k_y = k_z = 1$. Inset confirms that the oscillatory zone of thick line is continuous and smooth.

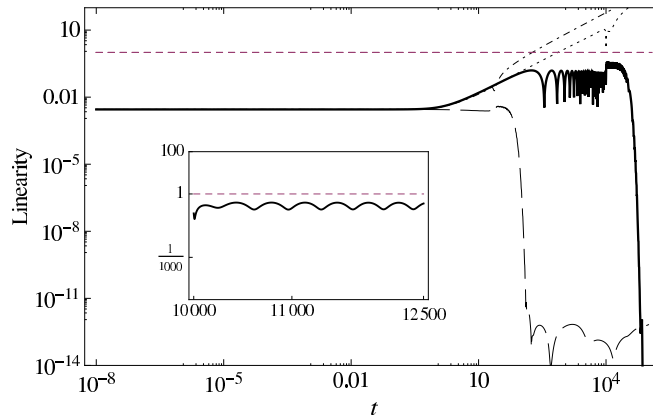


FIG. 5: Linearity of cases in Fig. 4. Dashed horizontal line indicates linearity unity. Inset confirms that the oscillatory zone of thick line is continuous and smooth.

of R_e and it is further suppressed above a certain higher \mathbf{B} (when indeed MRI is a weak field effect). At larger R_e , which actually corresponds to astrophysical accretion disks, growth rate due to TG overpowers that due to MRI. Although Fig. 6 represents cases corresponding to a vertical background magnetic field, we obtain similar trends of results at other background magnetic field geometries and wavevectors, and hence they are not shown here.

IV. COMPARISON OF PARAMETER SPACE FOR DIFFERENT INITIAL AMPLITUDE OF PERTURBATIONS

Figure 7 compares the parameter spaces, as described in Fig. 6, for two different IPAs: 10^{-3} and 10^{-5} . As IPA decreases, the value of R_e dividing the MRI active and TG active zones, namely R_{ed} , increases, which apparently implies that the MRI active region increases. It also appears that $R_{ed} \sim \text{IPA}^{-3}$. Let us now recall the time scale leading to the system to be nonlinear by the respective growths due to MRI and TG and estimate if those tally with observation and initial choice of our model. For this purpose, first we fix R_e at 10^{12} and take the IPA to be 10^{-3} , along with sufficiently low \mathbf{B} so that the flow is assured to be nonlinear and unstable, in the parameter space described in Figs. 6 and 7. In this case, nonlinearity arises in the TG active zone at about 750 rotation time and corresponding TG is shown in Fig. 5 (dotted line). If the shearing box is at $100R_g$ away from a $10M_\odot$ black hole, where R_g and M_\odot are Schwarzschild radius and Solar mass respectively, then this dimensionless time scale recasts into $750L/(q\Omega L) = 750\sqrt{R^3/GMq^2} \sim 750$ seconds for $q = 1.5$ (Keplerian disk), when L is the radial width of the shearing box, G the Newton's gravitation constant and M the mass of the black hole. Now if we decrease IPA to 10^{-5} keeping R_e fixed, TG cannot bring nonlinearity any more (however by increasing R_e , again TG could bring nonlinearity), as shown in Fig. 7, instead, the nonlinearity arises then via MRI modes. However, the time scale

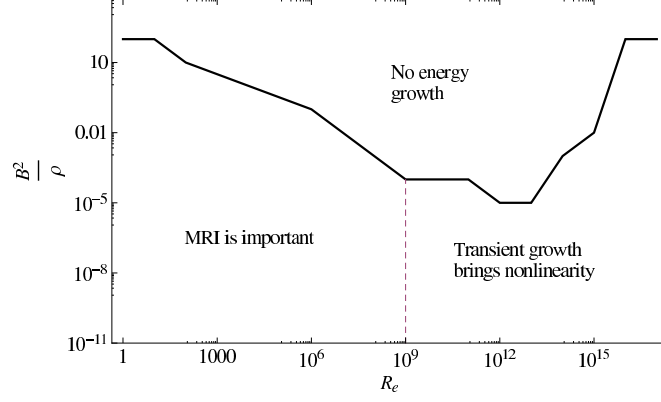


FIG. 6: Parameter space describing stable and unstable zones, based on the MRI and TG inactive and active regions, when $\mathbf{B} = (0, 0, B_3)$ and IPA is 10^{-3} . The dashed vertical line at $R_e = 10^9$ is the threshold R_e above which MRI does not work. $k_x^L = -R_e^{1/3}$, $k_y = k_z = 1$.

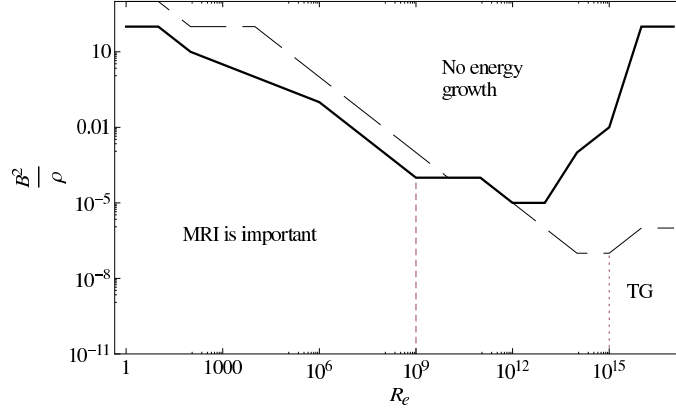


FIG. 7: Same as Fig. 6 but comparing results with different IPA, when solid and longdashed lines are for IPA = 10^{-3} and 10^{-5} respectively. The dashed and dotted vertical lines at $R_e = 10^9$ and 10^{15} correspond to threshold R_e (as in Fig. 6) when IPA = 10^{-3} and 10^{-5} respectively.

for the emergence of nonlinearity, in this MRI active process, as shown in Fig. 5, is approximately 35000 rotation time which is ~ 35000 seconds (following the same procedure, as used above for the TG active case, to convert the dimensionless to dimension-full times). Now we can calculate the radial velocity (v_r) of the Keplerian accretion disk at the location of shearing box for a given accretion rate \dot{M} , say 0.1 Eddington rate [20], which is supported by observation, given by [20]

$$v_r = 2 \times 10^6 \alpha^{4/5} \left(\frac{\dot{M}}{3 \times 10^{-8} M_\odot / \text{year}} \right)^{2/5} \left(\frac{M}{M_\odot} \right)^{-1/5} \left(\frac{R}{3R_g} \right)^{-2/5} \left[1 - \left(\frac{R}{3R_g} \right)^{-1/2} \right]^{-3/5}, \quad (24)$$

when α is the Shakura-Sunyaev viscosity parameter (whose origin is actually aimed here to determine). It is reasonable to assume that the time required to make the flow nonlinear, and hence turbulent which subsequently reveals viscosity, is of the same order as the time required by a fluid parcel to cross the length of the shearing box radially (t_L) as a result of turbulent viscosity. Hence, the product of v_r and t_L should be of the order of width of the shearing box L . For the above mentioned case of IPA = 10^{-3} , when nonlinearity is due to TG, we obtain $L = 0.1R_g$ from equation (24), which is highly reasonable for our choice of shearing box approximation ($L \ll R$). However, for the case of IPA = 10^{-5} , when nonlinearity is due to MRI, we obtain $L = 10R_g$ which marginally satisfies (or even violates) the initial choice of a narrow shearing box at $100R_g$. Therefore, although smaller IPAs increase MRI active zones, the observed infall cannot be explained by them. This problem with MRI would appear to be more severe at progressively lower IPAs and TG would be more important for revealing nonlinearity at progressively higher R_e , which are forbidden for MRI.

V. DISCUSSION AND CONCLUSIONS

Let us estimate the maximum $|\mathbf{B}|$ in Gauss supporting nonlinearity, as shown by the solid curve(s) in Figs. 6 and 7. We again set the shearing box at $100R_g$ away from a $10M_\odot$ black hole. Then we obtain the values of density (ρ_{100R_g}) at that location to be $\sim 10^{-4}$ gm/cc [20]. The background Keplerian velocity at that position, for the size of the shearing box, $0.1R_g$, which is consistent with that obtained for the TG active zone, can be obtained as $q\Omega L = q\sqrt{GM/R^3}L \sim 10^6$ cm/sec. We now consider $R_e = 10^{12}$ and, hence, from Fig. 6 the corresponding maximum (dimensionless) magnetic field supporting nonlinearity is given by $B^2/\rho = 10^{-5}$. Therefore, corresponding actual value of magnetic field is $\sqrt{10^{-5}\rho_{100R_g}(q\Omega L)^2} \sim 30$ Gauss. This means, the flow with $R_e = 10^{12}$ and $|\mathbf{B}| > 30$ Gauss, the energy growth of perturbation will decay over time, but for $|\mathbf{B}| \leq 30$ Gauss, TG will be sufficient enough to bring nonlinearity in the system, however, still not requiring any growth due to MRI. From Fig. 6, it is clear that MRI is only important whenever $R_e < 10^9$, whereas for $R_e \geq 10^9$, which is the favorable zone of R_e for accretion disks, magnetic TG is important than MRI.

In short, we have calculated the magnetic field strengths for different R_e s above which the system will be stable under linear perturbation and an upper bound of R_e above which either the system is stable under linear perturbation (for high magnetic field strength) or reaches nonlinear regime (for low magnetic field) through magnetic TG. In one line, MRI is not the sole mechanism to make accretion disk unstable, there is a big kingdom where TG rules, and explanation of accretion solely via MRI is misleading.

The authors would like to thank Prateek Sharma for illuminating discussion. B.M. acknowledges partial support through the research grant provided by Indian Space Research Organization of Ref. No. ISRO/RES/2/367/10-11.

-
- [1] J.E. Pringle, ARA&A **19**, 137 (1981).
 - [2] B. Mukhopadhyay, Phys. Lett. B **721**, 151 (2013).
 - [3] E. Velikhov, J. Exp. Theor. Phys. **36**, 1398 (1959).
 - [4] S. Chandrasekhar, Proc. Nat. Acad. Sci. (USA) **46**, 253 (1960).
 - [5] S.A. Balbus, and J.F. Hawley, Astrophys. J. **376**, 214 (1991).
 - [6] B. Mukhopadhyay, N. Afshordi, and R. Narayan, Astrophys. J. **629**, 383 (2005).
 - [7] N. Afshordi, B. Mukhopadhyay, and R. Narayan, Astrophys. J. **629**, 373 (2005).
 - [8] G.D. Chagelishvili, J.-P. Zahn, A.G. Tevzadze, J.G. Lominadze, Astron. Astrophys. **402**, 401 (2003).
 - [9] P.A. Yecko, Astron. Astrophys. **425**, 385 (2004).
 - [10] O.M. Umurhan, and O. Regev, Astron. Astrophys. **427**, 855 (2004).
 - [11] M. Avila, Phys. Rev. Lett. **108**, 124501 (2012).
 - [12] H.H. Klahr, and P. Bodenheimer, Astrophys. J. **582**, 869 (2003).
 - [13] S.M. Mahajan, V. Krishan, Astrophys. J. **682**, 602-607 (2008).
 - [14] O.M. Umurhan, K. Menou, and O. Regev, Phys. Rev. Lett. **98**, 034501 (2007).
 - [15] E. Liverts, Y. Shtemler, M. Mond, O.M. Umurhan, and D.V. Bisikalo, Phys. Rev. Lett. **109**, 224501 (2012).
 - [16] M.E. Pessah, and C. Chan, Astrophys. J. **751**, 48 (2012).
 - [17] J. Squire and A. Bhattacharjee, Phys. Rev. Lett. **113**, 025006 (2014).
 - [18] S.A. Balbus, and J.F. Hawley, Rev. Mod. Phys. **70**, 1 (1998).
 - [19] B. Mukhopadhyay, Astrophys. J. **653**, 503 (2006).
 - [20] N.I. Shakura, and R.A. Sunyaev, Astron. Astrophys. **24**, 337 (1973).